# Direct Calculation of *ZZ* Interaction Rates in Multimode Circuit Quantum Electrodynamics

Firat Solgun* and Srikanth Srinivasan
*IBM Quantum, IBM T. J. Watson Research Center, Yorktown Heights, New York 10598, USA*

(Received 19 November 2021; revised 20 July 2022; accepted 12 September 2022; published 11 October 2022)

Hamiltonians of the superconducting qubits of transmon type involve nonzero *ZZ* interaction terms due to their finite and small anharmonicities. These terms might lead to the unwanted accumulation of spurious phases during the execution of the two-qubit gates. Exact calculation of the *ZZ* interaction rates requires the full diagonalization of the circuit Hamiltonians, which very quickly becomes computationally demanding as the number of the modes in the coupler circuit increases. Here we propose a direct analytical method for the accurate estimation of the *ZZ* interaction rates between low-anharmonicity qubits in the dispersive limit of the multimode circuit quantum electrodynamics (circuit QED). We observe very good agreement between the predictions of our method and the measurement data collected from the multiqubit devices.

DOI: 10.1103/PhysRevApplied.18.044025

## I. INTRODUCTION

Superconducting quantum processors are one of the leading platforms in the race to achieve fault-tolerant quantum computation. Several performance figures, such as the qubit coherence times, and gate and measurement fidelities have been steadily improving in the last two decades and they reached [1–5] the error threshold levels as required by the quantum error-correction protocols [6,7]. However keeping the same performance for the individual components while scaling the circuits up remains a big engineering challenge [8].

Superconducting qubits are made of Josephson junctions, which are lossless two-terminal circuit elements. Josephson junctions provide the nonlinearity needed to obtain the qubit modes by allowing the "supercurrent" to flow between their terminals by tunneling while introducing minimal loss [9]. The most popular superconducting qubit transmon [10] is obtained by shunting the Josephson junction with a relatively large capacitor. As such, the transmon qubit is a nonlinear oscillator with small anharmonicity to make it insensitive to charge fluctuations that cause dephasing. Transmon qubits are often modeled as multilevel quantum Duffing oscillators and they are designed to interact with each other and with their environment in the circuit-QED architecture [11,12].

In the circuit-QED architecture, qubit interactions are mediated by the linear and passive microwave environment that the Josephson junctions are embedded in. Qubits are typically coupled to each other and to the control and measurement electronics by the help of microwave components constructed out of coplanar waveguide (CPW) transmission lines and their bare interactions with the internal modes of these structures are of the exchange energy type. When the strength of these interactions is smaller than the detuning of the qubits from the internal modes the system is said to be operated in the dispersive regime. It was shown in Ref. [13] that in the dispersive limit multimode circuit-QED systems can be described by an effective Hamiltonian of Duffing oscillators whose interactions with each other and with the drive lines are directly related to the entries of the impedance matrix defined between the qubit and drive ports.

However, when one reduces the effective Hamiltonian of the circuit to a qubit Hamiltonian by eliminating the higher levels of the Duffing oscillators' nonzero *ZZ* interaction (Ising-type) terms are generated due to the finite and small anharmonicities of the qubits in addition to the main exchange interaction terms [14]. These *ZZ* interaction terms might be a nuisance for some two-qubit gate schemes such as the CR gate [15], which is the most popular microwave-activated gate that creates the entanglement between the qubits via the *ZX* interaction. A nonzero *ZZ* term in the qubit Hamiltonian will cause spurious phase accumulations in the presence of spectator qubits and will lead to the loss of the gate fidelity.

The suppression of the *ZZ* term in the qubit Hamiltonians has recently been studied actively to improve two-qubit gate fidelities. In Ref. [16] a coupler design is proposed that consists of two arms, one of which is frequency tunable and the coupler suppresses the *ZZ* term by the interference of the interaction paths through each arm.

*fsolgun@us.ibm.com

 © 2022 American Physical Society

It is shown that the system can be tuned to a point where the *ZZ* interaction becomes zero but the effective exchange interaction $J$ remains finite. A similar topology was used in Ref. [17] to make exchange interaction zero. Other approaches include the use of qubits of opposite anharmonicities [18] and of tunable qubits [19] to cancel the *ZZ* interaction. More recently with a circuit topology similar to Ref. [16] but using nontunable elements only [20] showed that it is possible to suppress the *ZZ* term over a relatively large band while keeping a finite $J$-coupling rate that is useful for running the CR gate. Although a source of crosstalk for the CR gate *ZZ* interactions can also mediate controlled-phase (CZ) gates [21–27].

In this paper we develop a method for the accurate estimation of the *ZZ* rates between transmon-type low anharmonicity qubits in the multimode circuit QED. The frequency dependence of the *ZZ* rates is captured by the impedance entries connecting the qubit ports and hence the high computational cost of diagonalizing multimode Hamiltonians is avoided, making the microwave engineering [28] of multimode quantum couplers streamlined.

We start by describing our method in Sec. II. The predictions of our theory are validated with numerical simulations on the example circuits in Sec. III. In Sec. IV we compare the experimental data collected from multiqubit devices to the *ZZ* values calculated with our method. In Sec. A we give a summary of the theory [13] that our method is based on and the details of the derivation of the results reported in the main text below.

## II. CALCULATION OF THE *ZZ* INTERACTION RATES

We assume that we have a quantum processor consisting of $N$ transmon qubits coupled to each other with the help of a linear passive microwave network, which results in an effective exchange-energy interaction $J_{ij}$ between the qubits $i$ and $j$ as shown in Fig. 1 whose value is given by the formula [13]

$$J_{ij} = -\frac{1}{4}\sqrt{\frac{\omega_i\omega_j}{L_iL_j}}\,\mathrm{Im}\left[\frac{Z_{ij}\,(\omega_i)}{\omega_i}+\frac{Z_{ij}\,(\omega_j)}{\omega_j}\right], \tag{1}$$

where $\omega_i$, $\omega_j$ are qubit frequencies, $L_i$, $L_j$ qubit inductances, and $Z_{ij}$ is the impedance entry connecting the qubit ports. For a summary of the results in Ref. [13] where Eq. (1) is derived we refer the reader to Appendix A 1. The exchange coupling $J_{ij}$ in Eq. (1) can be diagonalized to get the following qubit Hamiltonian [14] (with $\hbar = 1$)

$$\hat{H}_q = -\frac{(\omega_{10}+\omega_{ZZ}/2)}{2}\hat{Z}\hat{I} - \frac{(\omega_{01}+\omega_{ZZ}/2)}{2}\hat{I}\hat{Z} + \frac{\omega_{ZZ}}{4}\hat{Z}\hat{Z}, \tag{2}$$

where $\omega_{10} = \omega_i + J_{ij}^2/\Delta_{ij}$ and $\omega_{01} = \omega_j - J_{ij}^2/\Delta_{ij}$ are the dressed qubit frequencies, $\Delta_{ij} = \omega_i - \omega_j$ is the detuning between the qubits and above we assume $J_{ij} \ll |\Delta_{ij}|$. The *ZZ* interaction rate $\omega_{ZZ}$ is shown to be [14]

$$\omega_{ZZ} = \omega_{11} - \omega_{10} - \omega_{01} \tag{3}$$

$$\approx -\frac{2J_{ij}^2(\delta_i+\delta_j)}{(\Delta_{ij}+\delta_i)(\delta_j-\Delta_{ij})}, \tag{4}$$

where $\delta_i$ and $\delta_j$ are qubit anharmonicities. However, the accuracy of the formula in Eq. (4) can be improved significantly if one inspects more closely the higher-order terms that are often dropped with a rotating-wave approximation and include in the treatment the terms that are rotating at much slower frequencies. Such terms will bring corrections to the couplings between the second excited states of the qubits $|20\rangle$, $|02\rangle$ and the $|11\rangle$ state as shown in the state diagram in Fig. 1. We define the nonlinear term $\hat{H}_\delta$ that collects such terms to be added to the total Hamiltonian $\hat{\mathcal{H}}$ in Eq. (A1) as given below

$$\hat{H}_\delta = \sum_{i,j}\delta_i\sqrt{\frac{\omega_i}{\omega_j}}\alpha_{ij}\hat{b}_i^\dagger\hat{b}_j^\dagger\hat{b}_i\hat{b}_i + \delta_j\sqrt{\frac{\omega_j}{\omega_i}}\alpha_{ji}\hat{b}_j^\dagger\hat{b}_i^\dagger\hat{b}_j\hat{b}_j + \text{h.c.}$$
$$+\,\omega_{ZZ}^{(K)}\hat{b}_i^\dagger\hat{b}_j^\dagger\hat{b}_i\hat{b}_j, \tag{5}$$

where h.c. stands for the Hermitian conjugate of the first two terms in the expression above and $\hat{b}_i$ is the annihilation operator of the $i$th qubit mode. The weight coefficients of the terms in Eq. (5) are given as functions of the off-diagonal entries $\alpha_{ij}$'s of the total coordinate transformation $\boldsymbol{\alpha} = \mathbf{T}\exp(\mathbf{S})$ defined in Ref. [13] and are given by

$$\alpha_{ij} = \frac{Z_{ji}^{-1}}{2(\omega_j^2-\omega_i^2)}\mathrm{Im}\left[(\omega_i^2-2\omega_j^2)Z_{ij}(\omega_j)+\omega_i\omega_j Z_{ij}(\omega_i)\right], \tag{6}$$

where the "cross-characteristic impedance" $Z_{ij}$ is defined by $Z_{ij} = \sqrt{L_i/C_j}$. The details of how we obtain $\hat{H}_\delta$ can be found in Appendix A 2.

Using the first two terms in Eq. (5) and Eq. (6) together with Eq. (1) above we can now write the couplings $J_{\delta_i}$ and $J_{\delta_j}$ shown in Fig. 1 as

$$J_{\delta_i} = -\frac{1}{4}\sqrt{\frac{\omega_i\omega_j}{L_iL_j}}\,\mathrm{Im}\left[\alpha_{\delta_i}^{(i)}\frac{Z_{ij}\,(\omega_i)}{\omega_i}+\alpha_{\delta_i}^{(j)}\frac{Z_{ij}\,(\omega_j)}{\omega_j}\right], \tag{7}$$

$$J_{\delta_j} = -\frac{1}{4}\sqrt{\frac{\omega_i\omega_j}{L_iL_j}}\,\mathrm{Im}\left[\alpha_{\delta_j}^{(i)}\frac{Z_{ij}\,(\omega_i)}{\omega_i}+\alpha_{\delta_j}^{(j)}\frac{Z_{ij}\,(\omega_j)}{\omega_j}\right], \tag{8}$$

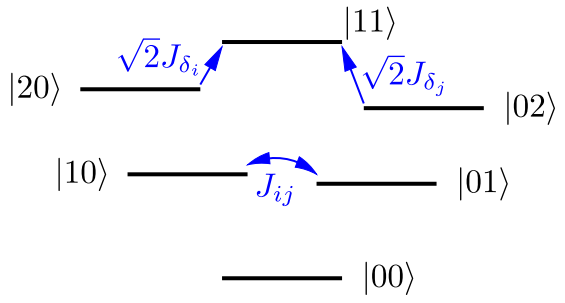


FIG. 1. State diagram of the two transmon qubits coupled with exchange coupling as given in Eq. (1). The couplings $J_{\delta_i}$, $J_{\delta_j}$ of the second excited states $|20\rangle$, $|02\rangle$ of the qubits to the state $|11\rangle$ are updated with the treatment of the higher-order terms in Eq. (5). Only states with up to two qubit excitations are shown and $|\Delta_{ij}| < |\delta_i|, |\delta_j|$, i.e., the straddling regime is assumed for simplicity with $\Delta_{ij} = \omega_i - \omega_j$ being the detuning between the qubits $i$ and $j$ and $\delta_i$, $\delta_j$ being qubit anharmonicities. Our treatment remains valid in the nonstraddling regime as well if the dispersive and low-anharmonicity conditions for the system are not violated.

where the correction factors $\alpha^{(i)}_{\delta_i}, \alpha^{(j)}_{\delta_i}, \alpha^{(i)}_{\delta_j}, \alpha^{(j)}_{\delta_j}$ are given by

$$\alpha^{(i)}_{\delta_i} = 1 + 2\frac{\omega_i \delta_i}{(\omega_i^2 - \omega_j^2)}, \tag{9}$$

$$\alpha^{(j)}_{\delta_i} = 1 - 2\frac{\omega_i \delta_i}{(\omega_i^2 - \omega_j^2)} + 4\frac{\delta_i}{\omega_i}, \tag{10}$$

$$\alpha^{(i)}_{\delta_j} = 1 + 2\frac{\omega_j \delta_j}{(\omega_i^2 - \omega_j^2)} + 4\frac{\delta_j}{\omega_j}, \tag{11}$$

$$\alpha^{(j)}_{\delta_j} = 1 - 2\frac{\omega_j \delta_j}{(\omega_i^2 - \omega_j^2)}. \tag{12}$$

Hence we can update the perturbative formula in Eq. (4) for the *ZZ* rate as

$$\omega^{(J)}_{ZZ} = 2\frac{J^2_{\delta_i}(\delta_j - \Delta_{ij}) + J^2_{\delta_j}(\delta_i + \Delta_{ij})}{(\Delta_{ij} + \delta_i)(\Delta_{ij} - \delta_j)}. \tag{13}$$

See Appendix A 4 for the derivation of the expressions given in Eqs. (7) and (8) for $J_{\delta_i}$ and $J_{\delta_j}$. We note that the formula in Eq. (13) gives a positive contribution to the total *ZZ* rate $\omega_{ZZ}$ defined in Eq. (3) in the straddling regime $|\Delta_{ij}| < |\delta_i|, |\delta_j|$ and reduces to the formula in Eq. (4) in the limit of $J_{\delta_i} = J_{\delta_j} = J_{ij}$.

Next we look at the last term in Eq. (5) that contributes to the value of the *ZZ* rate; in other words, the term $\omega^{(K)}_{ZZ} \hat{b}_i^\dagger \hat{b}_j^\dagger \hat{b}_i \hat{b}_j$, which is also called as the "cross-Kerr" term. Its contribution to the *ZZ* rate is negative, which is usually small in magnitude in the dispersive region. Its value $\omega^{(K)}_{ZZ}$ is calculated by working out the weight coefficients given in Eq. (A13) of Appendix A 2 to get

$$\omega^{(K)}_{ZZ} = 2\delta_i \left(\frac{\omega_i}{\omega_j}\right) \alpha^2_{ij} + 2\delta_j \left(\frac{\omega_j}{\omega_i}\right) \alpha^2_{ji} \tag{14}$$

so that we can write the total *ZZ* interaction rate $\omega_{ZZ}$ defined in Eq. (3) as

$$\omega_{ZZ} = \omega^{(J)}_{ZZ} + \omega^{(K)}_{ZZ}. \tag{15}$$

Finally, we introduce another parameter that was originally defined in Eq. (120) of Ref. [13]

$$\alpha_{ii} = \frac{1}{2} - \frac{3}{4}\mathrm{Im}[Z_{ii}(\omega_i)]/Z_i - \frac{1}{4}\omega_i \mathrm{Im}[Z'_{ii}(\omega_i)]/Z_i, \tag{16}$$

where $Z_i = \sqrt{L_i/C_i}$ is the characteristic impedance of the $i$th qubit and $Z'_{ii}(\omega_i) = dZ_{ii}(\omega)/d\omega|_{\omega=\omega_i}$. Note that this is an updated version of the expression given in Eq. (120) of Ref. [13]. The coefficient $\alpha_{ii}$ gives the weight of the flux of qubit mode $i$ on its own junction's phase. $\alpha_{ii} \cong 1$ in the dispersive region but it starts to deviate from one as the system exits the dispersive regime. Hence it is a good measure of how dispersive the system is. To include the corrections due to $\alpha_{ii}$'s into our treatment all we need to do is to replace the charging energy $E^{(i)}_C$ in the expression for the anharmonicity in Eq. (A3) with $\alpha^2_{ii} E^{(i)}_C$; in other words, we need to update the anharmonicity $\delta_i$ of the qubit $i$ given in Eq. (A3) as follows:

$$\delta_i = -\frac{\alpha^2_{ii} E^{(i)}_C}{1 - 2\alpha^2_{ii} E^{(i)}_C/\omega_i}. \tag{17}$$

The updated formula above for the anharmonicity $\delta_i$ allows us to capture the frequency-dependent changes due to the existence of the high-frequency modes coupled to the qubits. We refer the reader to Appendix A 3 for the derivation of the expressions given in Eqs. (16) and (17) for $\alpha_{ii}$ and $\delta_i$.

## III. NUMERICAL EXAMPLES

We apply the method developed in the previous section for the direct calculation of the *ZZ* rates to some simple circuits and compare the results to the exact diagonalization of the circuit Hamiltonians.

### A. Single-mode coupler

We start with the simple circuit shown in Fig. 2 consisting of two transmon qubits coupled via a single-mode shunt *LC* resonator bus. With $C_q = 60$ fF, $C_c = 5$ fF we fix the qubits at 5.0 and 5.2 GHz by adjusting the values of $L_{J_1}$ and $L_{J_2}$ accordingly and plot the *ZZ* interaction rate as a function of the bus-resonator frequency $f_b$ in Fig. 3

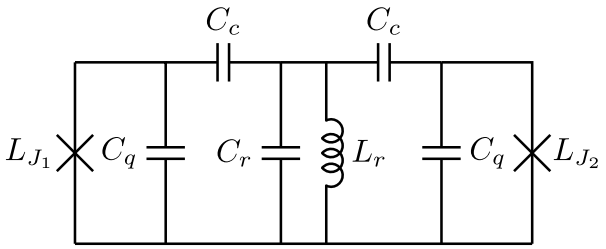


FIG. 2. Single-mode bus-circuit diagram. Transmon qubits of shunting capacitances $C_q$'s and Josephson junctions $L_{J_1}$ and $L_{J_2}$ are capacitively coupled with coupling capacitances $C_c$'s to a bus resonator with inductance $L_r$ and capacitance $C_r$. With capacitance values of $C_q = 60$ fF, $C_c = 5$ fF we fix the qubits at 5.0 and 5.2 GHz by adjusting the values of the junction inductances $L_{J_1}$ and $L_{J_2}$ accordingly and plot the $ZZ$ interaction rate as a function of the bus resonator frequency $f_b$ in Fig. 3 assuming a characteristic impedance of $Z_r = \sqrt{L_r/C_r} = 50\ \Omega$ for the bus resonator.

using three different methods. The "naive" method of calculating the $ZZ$ rate is to plug in the value of $J_{12}$ calculated using Eq. (1) into Eq. (4). However, we observe in Fig. 3(a) that there is significant discrepancy between this method (green curve labeled "Naive" in the legend) and the exact value of the $ZZ$ rate obtained with the numerical diagonalization of the circuit Hamiltonian (blue curve). And this discrepancy stays at a significant level even if we go deep into the dispersive region; in other words, as the bus frequency increases. However, the accuracy is improved considerably when we apply the updated formula for the $ZZ$ rate in Eq. (13) by using the values of $J_{\delta_1}$ and $J_{\delta_2}$ defined in Eqs. (7) and (8). This is plotted as "$Z$-method-0" in Fig. 3(a) in orange color. The inset plot informs us about the exchange coupling strength $J_{12}$ between the qubits as a function of the bus frequency calculated using the impedance formula in Eq. (1) for the same set of circuit parameters.

The accuracy of our calculation of the $ZZ$ rate can be improved further by adding the "cross-Kerr" contribution in Eq. (14) and the corrections due to the $\alpha_{ii}$ coefficients in Eqs. (16) and (17) into our treatment. The results are shown in Fig. 3(b) where we observe that the $ZZ$ rate calculated with the addition of the cross-Kerr term (brown curve) underestimates slightly the exact value (blue curve) whereas with the addition of $\alpha_{ii}$ corrections we obtain a very good agreement (dashed red) with true $ZZ$ values (blue) all the way down to $f_b = 5.6$ GHz, which is only 400 MHz away from one of the qubits.

### B. Two-mode coupler with two $J_{12}$ zeros

Here we apply our method to a coupler consisting of two finite frequency modes. We start by artificially creating the following *trans*-impedance response

$$Z_{12}(\omega) = \frac{A(\omega_{z_1}^2 - \omega^2)(\omega_{z_2}^2 - \omega^2)}{\omega(\omega_{p_1}^2 - \omega^2)(\omega_{p_2}^2 - \omega^2)} \tag{18}$$

with three poles at dc, $\omega_{p_1} = 4.0$ GHz, $\omega_{p_2} = 6.25$ GHz, and two zeros at $\omega_{z_1} = 4.5$ GHz and $\omega_{z_2} = 5.5$ GHz. The coefficient $A$ is set to the value of $-7.97 \times 10^{10}$. Assuming transmon shunt capacitances of 65 fF we obtain the results in Fig. 4.

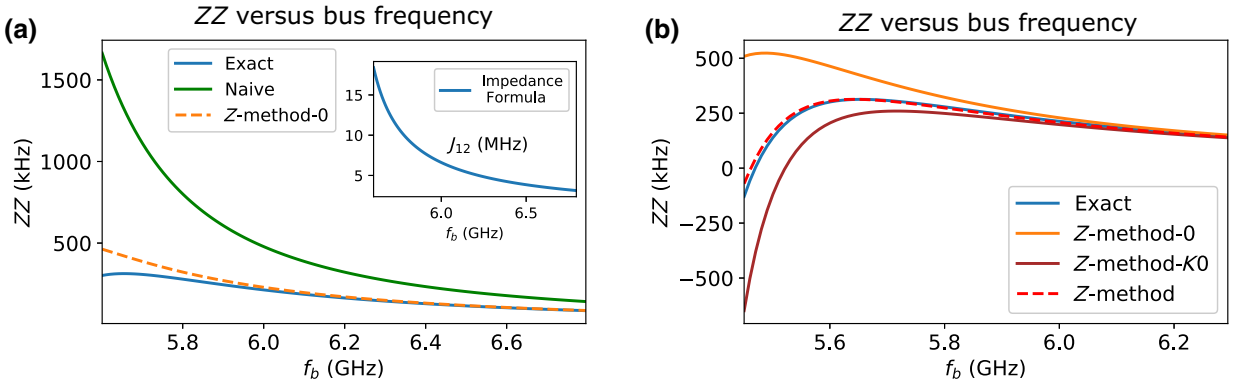


FIG. 3. (a) With qubits in Fig. 2 fixed at 5.0 and 5.2 GHz $ZZ$ rates calculated using the formula in Eq. (4) (labeled as "Naive" in the figure legend) and the formula in Eq. (13) (labeled as "$Z$-method-0" in the figure legend) are compared to the exact value by the numerical diagonalization of the circuit Hamiltonian (labeled as "Exact" in the figure legend). Inset shows the level of $J$ coupling as a function of the bus frequency plotted applying the impedance formula in Eq. (1). (b) For the example circuit in Fig. 2 with qubits fixed at 5.0 and 5.2 GHz when only the cross-Kerr contribution in Eq. (14) is added (brown curved labeled "$Z$-method-$K$0" in the legend) to the updated $ZZ$ formula in Eq. (13) (orange) we underestimate the exact $ZZ$ values (blue) slightly. However, when we also include the corrections due to the $\alpha_{ii}$ coefficients in Eqs. (16) and (17) we obtain the dashed red curve (labeled as "$Z$ method" in the figure legend), which agrees very well (even deep in the nondispersive region) with the exact $ZZ$ values (blue) obtained by a full diagonalization of the circuit Hamiltonian.

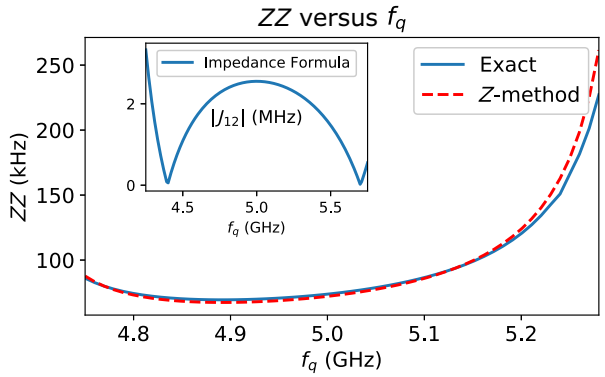


FIG. 4. *ZZ* rate for the *trans*-impedance $Z_{12}$ defined in Eq. (18) with one of the qubits set to 5.0 GHz while the other qubit's frequency is swept from 4.75 to 5.30 GHz. The exchange coupling strength $J_{12}$ is plotted in the inset for reference. Curves start diverging from each other after approximately 5.2 GHz because the qubit detuning becomes comparable to the anharmonicity.

### C. Nonlinear flux-tunable couplers

Before examining the multimode *ZZ* cancellation coupler in the next section and validating our method experimentally in the last Sec. IV here we illustrate with the help of two different qubit couplers, the extension of our method to the circuits employing nonlinear and flux-tunable elements.

#### *1. The gmon coupler*

We start with the gmon coupler circuit shown in Fig. 5, which was implemented in the superconducting quantum processor in Ref. [29] and analyzed theoretically in Ref. [30]. In these works transmon-type qubits are referred to as Xmons (due to their particular geometry) or gmons due their tunable couplings. In Fig. 5 two transmon qubits are inductively coupled to each other by introducing small linear inductors $L_{01}$ and $L_{02}$, which are shared in an inductive loop containing also a tunable Josephson junction $L_T$ tuned by the external flux $\Phi_{\text{ext}}$. By tuning the inductance $L_T$ one can make the effective impedance of the coupling junction $L_T$ very large to turn the coupling off.

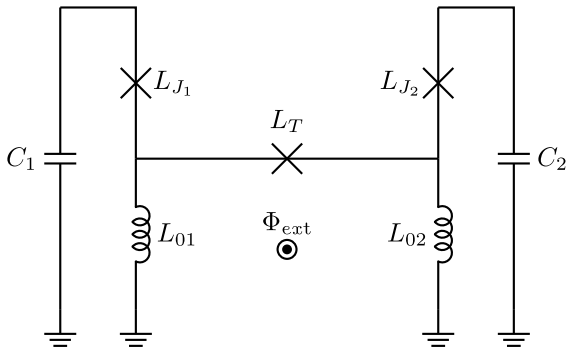


FIG. 5. Circuit representation of the two inductively coupled transmons (referred to also as $X$-mons or $g$-mons in Refs. [29, 30]) with the following circuit parameters: $C_1 = C_2 = 91$ fF, $L_{J_1} = L_{J_2} = 8.6$ nH, $L_{01} = L_{02} = 200$ pH, $L_T = 1.3$ nH as given in Ref. [30]. Flux bias $\Phi_{\text{ext}}$ is applied in the inductive loop to tune the effective inductance of the Josephson junction $L_T$. Note that it is assumed that both qubits are identical with equal frequencies in which case the exchange coupling $J_{12}$ between them is equal to the half of the splitting after the full diagonalization done in Fig. 6.

To be able to apply our method to the circuit in Fig. 5 we replace the coupler Josephson junction $L_T$ with an effective linear inductance $L_{\text{eff}} = L_T/\cos(\delta)$ where $\delta$ satisfies [30]

$$\delta + \left(\frac{L_{01} + L_{02}}{L_T}\right)\sin(\delta) = \phi_{\text{ext}}, \tag{19}$$

with $\phi_{\text{ext}} = 2\pi\,\Phi_{\text{ext}}/\Phi_0$, $\Phi_0$ being the flux quantum. Hence we obtain the circuit in Fig. 12 in Appendix A 5 with the coupler junction replaced with the effective linear inductance $L_{\text{eff}}$. In Eq. (A19) we give the two-port impedance matrix corresponding to the linearized gmon coupler circuit in Fig. 12 and apply the impedance method for the calculation of the *ZZ* rate to compare it to the exact diagonalization in Fig. (6) as a function of external flux. We see that our method accurately estimates the *ZZ* values obtained by exact diagonalization. For the details about the application of the impedance method to the nonlinear gmon circuit in Fig. 5 we refer the reader to Appendix A 5 a.

#### *2. Tunable bus coupler*

We now look at the flux-tunable bus-coupler circuit topology that has been recently studied and implemented in several works [21–26,31]. The circuit diagram is shown in Fig. 7.

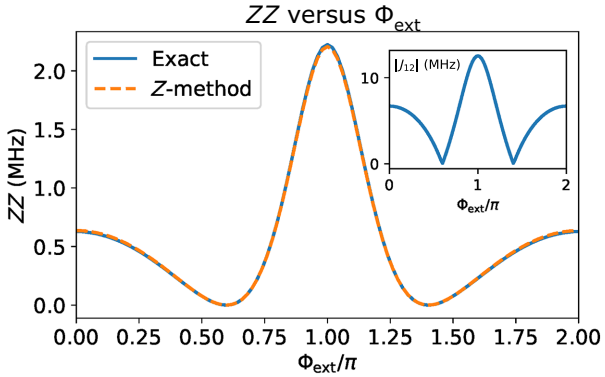


FIG. 6. *ZZ* rates calculated between gmon qubits in Fig. 5 as a function of the external flux bias $\phi_{\text{ext}}$. We observe very good agreement between the exact values (solid blue) and the values obtained by the application of our method (dashed orange). $J$-coupling level is given in the inset obtained from the half splitting of the degenerate qubit frequencies.

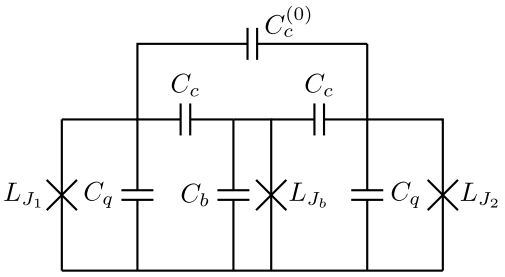


FIG. 7. Nonlinear flux-tunable bus-coupler circuit. Two transmon qubits are coupled via a flux-tunable nonlinear bus mode. The bus coupler junction $L_{J_b}$ is assumed to be tunable. The qubits are also coupled through a purely capacitive branch with the coupling capacitance $C_c^{(0)}$.

To apply our method we treat the coupler mode as a qubit mode and replace its bare junction inductance $L_{J_b}$ with an effective linear inductance $L_b = L_{J_b}/(1 - 2E_{C_b}/(\hbar\omega_b))$ as given in Ref. [13] to obtain the linear coupling network shown in Fig. 13. Here $E_{C_b} = e^2/[2(C_b + 2C_c)]$ is the charging energy corresponding to the coupler mode. Note that this is a valid approach as the coupler mode is operated in the transmon regime. Following the analysis in Appendix A 5 b of the effective coupling network in Fig. 13 we obtain the impedance entries and apply our method to calculate the $ZZ$ interaction values, which we compare with the exact values as shown in Fig. 8 with $C_q = C_b = 60$ fF, $C_c = 2.5$ fF, $C_c^{(0)} = 0.5$ fF.

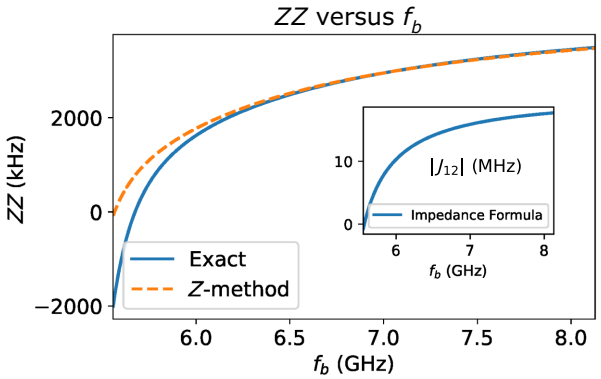


FIG. 8. $ZZ$ rate between the qubits in Fig. 7 obtained as a function of the bus-mode frequency by setting the qubit frequencies at 5.0 and 5.1 GHz and with the circuit parameter values of $C_q = C_b = 60$ fF, $C_c = 2.5$ fF, $C_c^{(0)} = 0.5$ fF in the circuit in Fig. 7. We note that these values lead to approximately 350 MHz of anharmonicity for the qubit and bus modes. Exact values obtained by the full diagonalization of the circuit Hamiltonian in the charge basis is shown in blue. $ZZ$ rates calculated by the application of our method using the impedance expressions in Eqs. (A22) and (A23) are shown in dashed orange. We observe satisfactory agreement in the dispersive region where the bus frequency is higher than 6.0 GHz.

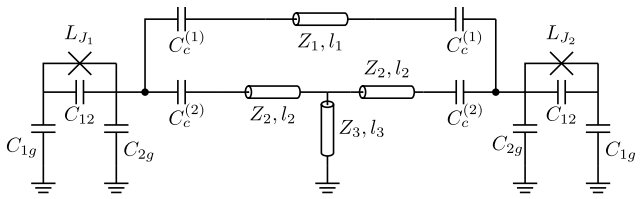


FIG. 9. Multimode $ZZ$ cancellation coupler circuit. The coupler consists of two arms: the top arm in the figure above is a short $\lambda/2$ CPW resonator whereas the bottom arm consists of a short CPW $\lambda/2$ section interrupted in the middle by a $\lambda/4$ resonator shorted to ground. Both arms run in parallel and are capacitively coupled to the same transmon qubit pads. Circuit parameters are $C_{12} = 36$ fF, $C_{1g} = C_{2g} = 46$ fF, $C_c^{(1)} = 8$ fF, $C_c^{(2)} = 12$ fF. CPW transmission lines have lengths $l_1 = 1.0$ mm, $l_2 = 0.5$ mm, $l_3 = 3.75$ mm, and center traces of width 10 um with 6 um gap to ground, which gives the characteristic impedances $Z_1 = Z_2 = Z_3 = 50\ \Omega$.

We note that although the agreement is satisfactory in the dispersive region for $f_b \gtrsim 6.0$ GHz as we move into the nondispersive region, i.e., for $f_b \leq 6.0$ GHz our estimates for the $ZZ$ values diverge quickly from the exact values. The reason for this discrepancy is the nonlinearity of the coupler junction that affects the $ZZ$ rates more significantly as the qubit modes hybridize strongly with the coupler mode in the nondispersive region.

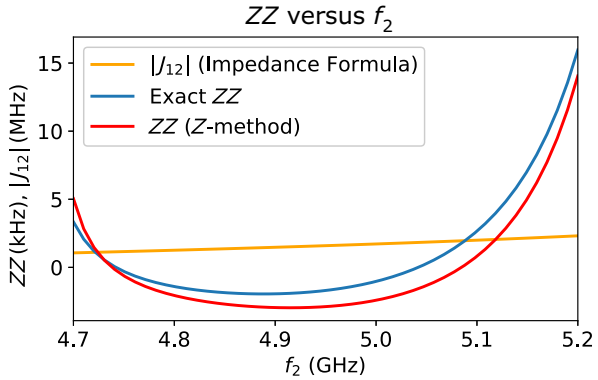


FIG. 10. $ZZ$ interaction rate (blue and red) and the exchange coupling rate $J_{12}$ (orange) for the coupler shown in Fig. 9 as functions of the second qubit's frequency with the first qubit set to 5.0 GHz. We again compare the exact value of the $ZZ$ rate to the value calculated by the impedance method applying the formula in Eq. (13) using Eqs. (7)–(12) and adding the cross-Kerr term in Eq. (14) together with the $\alpha_{ii}$ corrections, Eqs. (16) and (17). We observe good agreement at such a low level of $ZZ$ interaction and in the location of the first zero of $ZZ$ curves that happen at approximately 4.75 GHz. The second $ZZ$ zeros are slightly off as we approach the mode at approximately 6.3 GHz. We include the plot of the exchange coupling $J_{12}$, which is slowly increasing over the qubit band and reaches 2 MHz at approximately 5.10 GHz.

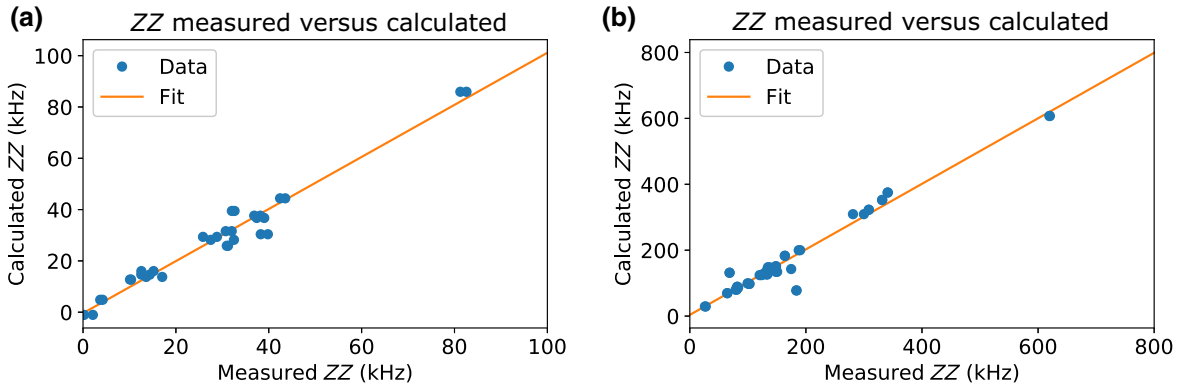


FIG. 11. (a) Scatter plot of the measured *ZZ* values in the multiqubit chip F609_C where qubit frequencies are spread over the band 4.8–5.0 GHz. The least-squares fit in the orange line has equation $y = 1.015x - 0.388$. The standard deviation is $\sigma = 3.7$ kHz. For each data point the $x$ value corresponds to the measured value whereas the $y$ value is the *ZZ* rate calculated using the impedance method. *ZZ* rates measured from both directions are included in the plot for each pair. (b) Scatter plot of the *ZZ* values for the Chip F608_C. *ZZ* values are larger by almost an order of magnitude compared to the chip F609_C in (a) since qubit frequencies are higher (in the band 5.0–5.2 GHz). The least-squares fit line is given by $y = 0.994x + 3.71$. The standard deviation is $\sigma = 28.5$ kHz. Again *ZZ* rates measured from both directions are included in the plot for each pair when available.

### D. Multimode *ZZ* cancellation coupler

In this section we study an example of a multimode coupler designed to cancel the *ZZ* interaction rate while keeping a finite $J$-coupling strength [20]. The coupler topology consists of two branches: one direct coupling branch of the form of a short segment of $\lambda/2$ CPW transmission line resonator and another branch of a short segment of CPW shunted to ground in the middle through a $\lambda/4$ CPW resonator. These two branches run in parallel and are connected to the same transmon qubit pads as shown in Fig. 9. The $\lambda/4$ section generates a mode at approximately 6.3 GHz. In Fig. 10 we plot *ZZ* interaction rate for qubits coupled by the circuit in Fig. 9. *ZZ* rate admits two zeros at approximately 4.75 GHz and approximately 5.04 GHz and remains small in magnitude in between, which is the typical qubit band.

## IV. EXPERIMENTAL RESULTS

In this section we test the validity of the analytical methods we develop in the previous sections on the measurement data collected from real devices. In Figs. 11(a) and 11(b) we compare the *ZZ* values predicted by our method to the measured values from two different multiqubit devices with qubit frequencies spread over two different frequency bands: on chip F609_C qubit frequencies fall in the band 4.8–5.0 GHz whereas qubits on chip F608_C lie between 5.0–5.2 GHz. Each chip contains 27 transmon qubits connected by the *ZZ* cancellation-type couplers introduced in Ref. [20]. We study this type of coupler in Sec. III D as an example to compare the results obtained by our analytical method to the exact *ZZ* rate values computed by the full diagonalization of the circuit Hamiltonian. Note that the *ZZ* cancellation effect is not observed since the cancellation band is missed in these chips. The coupler topology stays the same across the chip in the sense that all couplers consist of two short $\lambda/2$ CPW arms in parallel with one of the arms shorted to ground in the middle with a $\lambda/4$ CPW section. However, the length and the characteristic impedance of the arms and the resonance frequency of the $\lambda/4$ resonator differ creating six different coupler responses, which allows us to validate our analytical methods over a larger ensemble with the good agreement seen in Fig. 11. The calculated *ZZ* values are obtained using the $Z_{12}$ output of the 2.5D microwave simulations evaluated at the qubit frequencies. Self-capacitances $C_{J_i}$'s of the Josephson junctions are extracted (from the anharmonicity data) to be 3.0 fF for the chip F609_C and 2.2 fF for the chip F608_C as the chip F609_C had junctions with larger area.

## V. CONCLUSION

We describe a method for the accurate calculation of the *ZZ* rates between superconducting qubits in the multimode circuit QED. By relating the *ZZ* interaction rates directly to the impedance entries connecting the qubit ports our method allows streamlined analysis and design of the qubit-qubit couplers with the help of microwave simulations. In particular, this opens a path for the design of higher-order multipole *ZZ* cancellation couplers by avoiding computationally intensive multimode quantum Hamiltonian diagonalization.

## ACKNOWLEDGMENTS

F.S. acknowledges support from Intelligence Advanced Research Projects Activity (IARPA) under Contract No. W911NF-16-1-0114-FE.

## APPENDIX

### 1. The effective Hamiltonian

We start with an overview of the results in Ref. [13] as our calculations for the estimation of the $ZZ$ rates is performed in the reference frame given by the effective Hamiltonian derived in Ref. [13]. We assume that the quantum device under study consists of $N$ transmon qubits connected to each other and to the readout and control lines with the help of linear and passive microwave components, such as transmission lines. For such systems, the following effective Hamiltonian is derived in Ref. [13] in the dispersive limit of the circuit QED:

$$\hat{\mathcal{H}}/\hbar = \hat{H}_Q + \hat{H}_\chi + \hat{H}_R \tag{A1}$$

$\hat{\mathcal{H}}$ is obtained by block diagonalizing the initial system Hamiltonian in Eq. (17) of Ref. [13] by applying a Schrieffer-Wolff transformation. $\hat{H}_Q$ collects the terms corresponding to the qubit subspace:

$$\hat{H}_Q = \hat{H}_Q^D + \hat{H}_Q^J + \hat{H}_Q^V$$

where $\hat{H}_Q^D$ is the diagonal part:

$$\hat{H}_Q^D = \sum_{i=1}^{N} \omega_i \hat{b}_i^\dagger \hat{b}_i + \frac{\delta_i}{2} \hat{b}_i^\dagger \hat{b}_i (\hat{b}_i^\dagger \hat{b}_i - 1), \tag{A2}$$

which is the quantum Hamiltonian of $N$ Duffing oscillators of frequencies $\omega_i$'s, anharmonicities $\delta_i$'s and annihilation (creation) operators $\hat{b}_i(\hat{b}_i^\dagger)$'s; for $1 \le i \le N$. The anharmonicity $\delta_i$ of the qubit $i$ is given by [13]

$$\delta_i = -E_C^{(i)} \left(\frac{\omega_{J_i}}{\omega_i}\right)^2 = -\frac{E_C^{(i)}}{1 - 2E_C^{(i)}/\omega_i}, \tag{A3}$$

where $E_C^{(i)} = e^2/2C_i$ is the charging energy and $C_i$ is the total effective transmon shunting capacitance of the $i$th qubit; for $1 \le i \le N$. $\omega_{J_i} = 1/\sqrt{L_{J_i} C_i}$ with $L_{J_i}$ being the bare junction inductance corresponding to the $i$th qubit. $L_i$ is the inductance of the $i$th qubit and is related to the bare junction inductance $L_{J_i}$ by $L_i = L_{J_i}/[1 - (2E_C^{(i)}/\hbar\omega_i)]$, such that the qubit frequency $\omega_i$ is given by $\omega_i = \sqrt{L_i C_i}$.

Exchange couplings between qubits is given by the term $\hat{H}_Q^J$

$$\hat{H}_Q^J = \sum_{i,j} J_{ij} (\hat{b}_i \hat{b}_j^\dagger + \hat{b}_i^\dagger \hat{b}_j), \tag{A4}$$

where the following formula is derived in Ref. [13] for the exchange coupling $J_{ij}$ between qubit modes $i$ and $j$

$$J_{ij} = -\frac{1}{4}\sqrt{\frac{\omega_i \omega_j}{L_i L_j}} \mathrm{Im}\left[\frac{Z_{ij}(\omega_i)}{\omega_i} + \frac{Z_{ij}(\omega_j)}{\omega_j}\right], \tag{A5}$$

where $Z_{ij}$ is the impedance entry connecting the qubit port $i$ to the qubit port $j$. Qubit ports are defined across the Josephson junctions of the transmon qubits: port currents are the currents flowing through and the port voltages are the voltages developed across the Josephson junctions.

The term $\hat{H}_Q^V$ couples the qubits to the voltage drives and is given by

$$\hat{H}_Q^V = \sum_{i=1}^{N} \sum_{d=1}^{N_D} \varepsilon_{id} (\hat{b}_i - \hat{b}_i^\dagger) V_d. \tag{A6}$$

Here $V_d$ is the voltage source driving the $d$th drive line and there are $N_D$ voltage sources in total. $\varepsilon_{id}$ determines the coupling rate of the $i$th qubit to the voltage source $V_d$

$$\varepsilon_{id} = \sqrt{\frac{\omega_i}{2\hbar L_i}} \mathrm{Im}\left[Z_{i,p(d)}(\omega_i)\right] \frac{e^{i\theta_d} C_{p(d)}}{\sqrt{1 + \omega_d^2 Z_0^2 C_{p(d)}^2}}, \tag{A7}$$

where $Z_{i,p(d)}(\omega_i)$ is the impedance entry (evaluated at the frequency $\omega_i$ of the qubit $i$) connecting the qubit port $i$ to the drive port $p(d)$ corresponding to the voltage source $V_d$. $C_{p(d)}$ is the capacitance shunting the drive port $p(d)$ and $Z_0$ is the characteristic impedance of the drive line. $\omega_d$ is the frequency of the voltage source $V_d$, which is assumed to be a pure sinusoidal signal for simplicity. $\theta_d = (\pi/2) - \arctan(\omega_d Z_0 C_{p(d)})$ is the phase factor corresponding to $V_d$. See Ref. [13] for the details about the circuit model (the multiport Cauer network) used to define the qubit and drive ports.

$\hat{H}_R$ collects the terms corresponding to the modes of the linear passive environment that the qubits are embedded in

$$\hat{H}_R = \hat{H}_R^D + \hat{H}_R^J + \hat{H}_R^V, \tag{A8}$$

where $\hat{H}_R^D$ is the diagonal part given by

$$\hat{H}_R^D = \sum_{k=1}^{M} \omega_{R_k} \hat{a}_k^\dagger \hat{a}_k + \frac{\chi_{kk}^{(R)}}{2} \hat{a}_k^\dagger \hat{a}_k (\hat{a}_k^\dagger \hat{a}_k - 1). \tag{A9}$$

Here it is assumed that there are $M$ internal modes with the annihilation (creation) operators $\hat{a}_k^{(\dagger)}$'s and frequencies $\omega_{R_k}$'s. We note that the internal modes have acquired anharmonicities $\chi_{kk}^{(R)}$'s generated by the junction nonlinearities and described by the self-Kerr terms in Eq. (A9) above.

Similar to the case for the qubit modes the term $\hat{H}_R^J$ in Eq. (A8) gives the exchange coupling $J_{kk'}$ between the internal modes $k$ and $k'$

$$\hat{H}_R^J = \sum_{k,k'} J_{kk'} (\hat{a}_k \hat{a}_{k'}^\dagger + \hat{a}_k^\dagger \hat{a}_{k'}) \tag{A10}$$

and the term $\hat{H}_R^V$ couples the internal modes to the voltage drives

$$\hat{H}_R^V = \sum_{k=1}^{M}\sum_{d=1}^{N_D} \varepsilon_{kd}(\hat{a}_k - \hat{a}_k^\dagger)V_d. \tag{A11}$$

$\hat{H}_\chi$ holds the Kerr-type coupling terms left after the block diagonalization. In particular, the terms generating the qubit-state-dependent frequency shifts $\chi_{ik}$'s in the readout resonator frequencies are contained in $\hat{H}_\chi$ given by

$$\hat{H}_\chi = \sum_{i=1}^{N}\sum_{k=1}^{M} \chi_{ik}\hat{b}_i^\dagger\hat{b}_i\hat{a}_k^\dagger\hat{a}_k. \tag{A12}$$

### 2. Treatment of the nonlinear terms

To find the higher-order corrections to the theory presented in the previous section necessary for the accurate calculation of the *ZZ* interaction rates we borrow here the fourth-order expansion of the cosine potentials of the Josephson junctions used in Eq. (115) of Ref. [13] after normal ordering as

$$\begin{aligned}\hat{H}_\beta = -\sum_{pp'qq'} \beta_{pp'qq'}(&6\hat{a}_p^\dagger\hat{a}_{p'}^\dagger\hat{a}_q\hat{a}_{q'} + 4\hat{a}_p^\dagger\hat{a}_{p'}^\dagger\hat{a}_q^\dagger\hat{a}_{q'} \\ &+ 4\hat{a}_p^\dagger\hat{a}_{p'}\hat{a}_q\hat{a}_{q'} + \hat{a}_p\hat{a}_{p'}\hat{a}_q\hat{a}_{q'} + \hat{a}_p^\dagger\hat{a}_{p'}^\dagger\hat{a}_q^\dagger\hat{a}_{q'}^\dagger),\end{aligned} \tag{A13}$$

where $\hat{a}_p$ is the annihilation operator of the mode $p$ in the system, which can either be a qubit mode or a resonator mode. We distinguish below the qubit operators by reserving the symbol "$b$" for their operators such that $\hat{b}_i$ represents the annihilation operator of the $i$th qubit mode in the expansion in Eq. (A13). This expansion was originally given in Ref. [32] in a frame different than our block diagonal frame in Ref. [13]. Anharmonicity terms in the diagonal Duffing Hamiltonian in Eq. (A2) and the $\chi$-shift term $\hat{H}_\chi$ in the Hamiltonian in Eq. (A12) are both generated by $\hat{H}_\beta$ in Eq. (A13). To obtain the corrections to the couplings between $|20\rangle$, $|02\rangle$, and $|11\rangle$ states as shown in Fig. 1 we need to consider the terms $\hat{b}_i^\dagger\hat{b}_j^\dagger\hat{b}_i\hat{b}_i$, $\hat{b}_j^\dagger\hat{b}_i^\dagger\hat{b}_j\hat{b}_j$ and their Hermitian conjugates $\hat{b}_i^\dagger\hat{b}_i^\dagger\hat{b}_i\hat{b}_j$, $\hat{b}_j^\dagger\hat{b}_j^\dagger\hat{b}_j\hat{b}_i$, respectively, in Eq. (A13) above. Note that these terms are rotating (if one goes to the interaction picture, for example) at the frequency of qubit detuning $\Delta_{ij}$, which is much slower compared to the other terms. We collect these terms under the following nonlinear Hamiltonian term $\hat{H}_\delta$ that is to be added to the total Hamiltonian defined in Eq. (A1):

$$\begin{aligned}\hat{H}_\delta = \sum_{i,j}\delta_i\sqrt{\frac{\omega_i}{\omega_j}}\alpha_{ij}\hat{b}_i^\dagger\hat{b}_j^\dagger\hat{b}_i\hat{b}_i + \delta_j\sqrt{\frac{\omega_j}{\omega_i}}\alpha_{ji}\hat{b}_j^\dagger\hat{b}_i^\dagger\hat{b}_j\hat{b}_j + \text{h.c.} \\ + \omega_{ZZ}^{(K)}\hat{b}_i^\dagger\hat{b}_j^\dagger\hat{b}_i\hat{b}_j,\end{aligned} \tag{A14}$$

where "h.c." stands for the Hermitian conjugate of the first two terms in the first line above. The term in the second line above gives the cross-Kerr contribution to the total *ZZ* rate and its coefficient $\omega_{ZZ}^{(K)}$ is given by

$$\omega_{ZZ}^{(K)} = 2\delta_i\left(\frac{\omega_i}{\omega_j}\right)\alpha_{ij}^2 + 2\delta_j\left(\frac{\omega_j}{\omega_i}\right)\alpha_{ji}^2. \tag{A15}$$

The weights of the terms in the expression in Eq. (A14) above are calculated by working out the weight coefficients $\beta_{pp'qq'}$ given in Eq. (A13) in the reference frame of Ref. [13] with

$$\alpha_{ij} = \frac{Z_{ji}^{-1}}{2(\omega_j^2 - \omega_i^2)}\text{Im}\left[(\omega_i^2 - 2\omega_j^2)Z_{ij}(\omega_j) + \omega_i\omega_j Z_{ij}(\omega_i)\right]. \tag{A16}$$

Here we introduce the "cross-characteristic impedance" $Z_{ij} = \sqrt{L_i/C_j}$. The expression above is an update to the expression for $\alpha_{ij}$ originally given in Eq. (121) of Ref. [13] and is calculated using the total coordinate transformation $\boldsymbol{\alpha} = \mathbf{T}\exp(\mathbf{S})$ of Ref. [13]. See Appendix A 3 for the details of the derivation of the expression for $\alpha_{ij}$ in Eq. (A16).

### 3. Derivation of the expressions for $\alpha_{ij}$, $\alpha_{ii}$, and $\delta_i$

The expressions given in Eqs. (6) and (16) for the coefficients $\alpha_{ij}$ and $\alpha_{ii}$ can be derived by expanding the total coordinate transformation $\boldsymbol{\alpha} = \mathbf{T}\exp(\mathbf{S})$ given in Ref. [13] to second order in $\mathbf{S}$. Here $\boldsymbol{\alpha}$, $\mathbf{T}$, and $\mathbf{S}$ are all $(N+M)\times(N+M)$ matrices, where $N$ is the number of qubits and $M$ is the number of the internal modes. The coordinate transformation $\mathbf{T}$ is defined in Eq. (21) of Ref. [13] as

$$\mathbf{T} = \begin{pmatrix}\mathbf{1}_{N\times N} & \mathbf{C}_0^{1/2}\mathbf{R}^T \\ \mathbf{0}_{M\times N} & \mathbf{1}_{M\times M}\end{pmatrix}, \tag{A17}$$

where $\mathbf{C}_0$ is the diagonal matrix of transmon capacitances $(C_1,\ldots,C_N)$ and $\mathbf{R} = [r_{ik}]$ is the $N\times M$ turns-ratio matrix of the multiport Belevitch transformers in the canonical multiport Cauer network used in Ref. [13]. The matrix $\mathbf{S}$ defines the Schrieffer-Wolff transformation $\exp(\mathbf{S})$ that block diagonalizes the matrix $\mathbf{M}_1$ defined in Eq. (23) of Ref. [13] by

$$\begin{aligned}\mathbf{M}_1 &= \mathbf{T}^T\mathbf{C}_0^{-1/2}\mathbf{M}_0\mathbf{C}_0^{-1/2}\mathbf{T} \\ &= \begin{pmatrix}\Omega_J^2 & \Omega_J^2\mathbf{C}_0^{1/2}\mathbf{R}^T \\ \mathbf{R}\mathbf{C}_0^{1/2}\Omega_J^2 & \Omega_{R'}^2\end{pmatrix},\end{aligned} \tag{A18}$$

where $\Omega_J$ is the $N\times N$ diagonal matrix holding the qubit frequencies whereas the $M\times M$ matrix $\Omega_{R'}$ corresponds to the subspace of the internal modes. $\mathbf{M}_0$ is the diagonal matrix with entries $\left(1/L_1,\ldots,1/L_N,1/L_{R_1},\ldots,1/L_{R_M}\right)$

where $L_i$'s are qubit inductances for $1 \leq i \leq N$ and $L_{R_k} = 1/\omega_{R_k}^2$ are the inductances of the internal modes for $1 \leq k \leq M$.

After expanding $\exp(\mathbf{S})$ to second order in $\mathbf{S}$ using, for example, Eqs. (B.12) and (B.15) in Ref. [33] we obtain the expressions in Eqs. (A16) and (16) for the coefficients $\alpha_{ij}$ and $\alpha_{ii}$ from the $(i,j)$ and $(i,i)$ entries, respectively, of the upperleft $N \times N$ subsector of $\mathbf{T}\exp(\mathbf{S})$ corresponding to the qubit subspace.

The updated expression in Eq. (17) for the anharmonicity $\delta_i$ can be derived by noting that the capacitance rescaling performed by the diagonal matrix $\mathbf{C}_0^{-1/2}$ can be lumped into the total coordinate transformation $\boldsymbol{\alpha}$, which would renormalize the diagonal capacitance $C_i$ by $1/\alpha_{ii}^2$ hence the charging energy $E_C^{(i)}$ gets updated by the prefactor $\alpha_{ii}^2$; in other words, $E_C^{(i)} \to \alpha_{ii}^2 E_C^{(i)}$. One then obtains $\delta_i = -[\alpha_{ii}^2 E_C^{(i)}/(1 - 2\alpha_{ii}^2 E_C^{(i)}/\omega_i)]$ for the anharmonicity using the updated charging energy in the formula given in Eq. (A3).

#### 4. Derivation of the expressions for $J_{\delta_i}$ and $J_{\delta_j}$

The expression given in Eq. (7) for $J_{\delta_i}$ is obtained by noting that the term $\hat{b}_i^\dagger \hat{b}_j^\dagger \hat{b}_i \hat{b}_i$ and its Hermitian conjugate $\hat{b}_i^\dagger \hat{b}_i^\dagger \hat{b}_i \hat{b}_j$, which have weight $\delta_i \sqrt{(\omega_i/\omega_j)}\alpha_{ij}$ in the nonlinear Hamiltonian term $\hat{H}_\delta$ given in Eq. (A14) couple the state $|20\rangle$ to the state $|11\rangle$ with strength $\sqrt{2}\delta_i\sqrt{(\omega_i/\omega_j)}\alpha_{ij}$. This brings an additive correction to the main coupling $\sqrt{2}J_{ij}$ between the states $|20\rangle$ and $|11\rangle$ generated by the exchange coupling $J_{ij}$ given by the expression in Eq. (1) between qubits $i$ and $j$; in other words, $J_{\delta_i} = J_{ij} + \delta_i\sqrt{(\omega_i/\omega_j)}\alpha_{ij}$. After rearrangement we arrive at the expression given in Eq. (7) for $J_{\delta_i}$. A similar analysis applied to the terms $\hat{b}_j^\dagger \hat{b}_i^\dagger \hat{b}_j \hat{b}_j$ and $\hat{b}_j^\dagger \hat{b}_j^\dagger \hat{b}_j \hat{b}_i$ (with weight $\delta_j\sqrt{(\omega_j/\omega_i)}\alpha_{ji}$) for the coupling between the states $|02\rangle$ and $|11\rangle$ gives the expression in Eq. (8) for $J_{\delta_j}$.

#### 5. Nonlinear flux-tunable circuit analysis

##### a. The gmon coupler

Below we calculate the off-diagonal impedance entry for the two-port network shown in Fig. 12. The two-port impedance matrix is

$$\mathbf{Z}(\omega) = \frac{1}{j\omega}\begin{pmatrix} 1/C_1 & 0 \\ 0 & 1/C_2 \end{pmatrix} + j\omega \begin{pmatrix} L_{11} & L_{12} \\ L_{12} & L_{22} \end{pmatrix}, \quad \text{(A19)}$$

where $L_{11} = L_{22} = [L_0(L_{\text{eff}} + L_0)/(L_{\text{eff}} + 2L_0)]$, $L_{12} = [L_0^2/(L_{\text{eff}} + 2L_0)]$, and $L_0 = L_{01} = L_{02}$. We note here that the off-diagonal impedance is given by $Z_{12} = j\omega L_{12} = j\omega L_0^2/(L_{\text{eff}} + 2L_0)$ and the impedance matrix has the purely inductive term corresponding to infinite frequency [last term in Eq. (A19) above]. The diagonal part of this term introduces extra degrees of freedom corresponding to the flux variables across the small inductors $L_{01}$ and $L_{02}$. The rigorous way to treat these extra degrees of freedom is to eliminate them by applying the Born-Oppenheimer approximation since the resonance frequencies of the modes generated by the small inductors $L_{01}$ and $L_{02}$ will be very high. Here we simply combine $L_{01}$ and $L_{02}$ in series with the linear Josephson inductances $L_{J_1}$ and $L_{J_2}$ to get the following equation for the qubit frequencies:

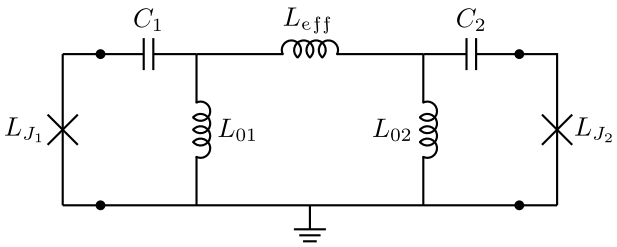


FIG. 12. Circuit equivalent to the circuit in Fig. 5 with the coupler junction $L_T$ replaced with an effective linear inductor $L_{\text{eff}} = L_T/\cos(\delta)$ where $\delta$ satisfies Eq. (19). Qubits with Josephson junctions $L_{J_1}$ and $L_{J_2}$ are coupled to each other in a purely inductive way through the passive two-port network with ports defined across the terminals of the junctions $L_{J_1}$ and $L_{J_2}$ shown with black dots.

$$x^2 = \left(\frac{L_J}{L_{11} + L_J} - 2r/x\right), \quad \text{(A20)}$$

where $x = \omega_q/\omega_J$, $\omega_q$ being the qubit frequency, $r = E_C/(\hbar\omega_J)$ with $L_J = L_{J_1} = L_{J_2}$ and $\omega_J = 1/\sqrt{L_J C_q}$ with $C_q = C_1 = C_2$. We note here that this is a slightly modified version of the Eq. (143) in Ref. [13] due to the existence of the small inductances $L_{01}$ and $L_{02}$ corresponding to the infinite frequency term in the partial-fraction expansion of the impedance in Eq. (A19) above. Now we apply the impedance formula in Eq. (1) of the text to get

$$J_{12} = -\frac{1}{2}\frac{\omega_q}{L_q}\left(\frac{L_0^2}{2L_0 + L_{\text{eff}}}\right), \quad \text{(A21)}$$

where $L_q$ is the linear qubit inductance $L_q = L_J/[L_J/(L_{11} + L_J)] - 2E_C/(\hbar\omega_q))$. Note that this relation is also a slightly modified version (due to the inductances $L_{01}$ and $L_{02}$) of the relation in Eq. (141) of Ref. [13].

##### b. The tunable bus coupler

By defining the ports across the terminals (black dots) of the junctions $L_{J_1}$, $L_{J_2}$ in Fig. (13) we calculate the two-port impedance matrix of the coupling network with the

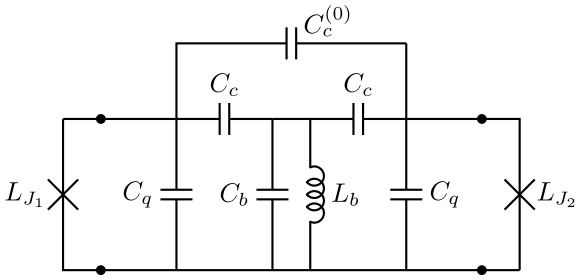


FIG. 13. Effective linear coupling network obtained for the tunable bus circuit in Fig. 7 by replacing the Josephson junction $L_{J_b}$ of the coupler mode with the effective linear inductance $L_b = L_{J_b}/(1 - 2E_{C_b}/(\hbar\omega_b))$.

following entries:

$$Z_{11}(s) = Z_{22}(s) = \frac{1}{(C_q + C_c')s} + Z_{12}(s), \tag{A22}$$

$$Z_{12}(s) = Z_{21}(s) = \frac{(C_c'/C_a)^2}{(C_q + C_c')s} + \left(\frac{C_0 C_c'}{C_a^2}\right)^2 \frac{s/C_b'}{(s^2 + \omega_b^2)}, \tag{A23}$$

where $C_0 = 2C_c + C_c^2/C_c^{(0)}$, $C_c' = C_c + 2C_c^{(0)}$, $C_a = \sqrt{(2C_c' + C_0)C_q + C_0 C_c'}$, $C_b' = C_b + 2(C_0 C_c' C_q/C_a^2)$, and $\omega_b = 1/\sqrt{C_b' L_b}$. Choosing the circuit parameter values of $C_q = C_b = 60$ fF, $C_c = 2.5$ fF, $C_c^{(0)} = 0.5$ fF and setting the qubits at 5.0 and 5.1 GHz we obtain the *ZZ* plots in Fig. (8) as a function of the frequency of the bus mode where we compare the exact value obtained with the diagonalization of the circuit Hamiltonian to the values obtained by the application of our method using impedance functions in Eqs. (A22) and (A23) above.


[1] A. D. Córcoles, E. Magesan, S. J. Srinivasan, A. W. Cross, M. Steffen, J. M. Gambetta, and J. M. Chow, Demonstration of a quantum error detection code using a square lattice of four superconducting qubits, Nat. Commun. **6**, 6979 (2015).

[2] S. Sheldon, E. Magesan, J. M. Chow, and J. M. Gambetta, Procedure for systematically tuning up crosstalk in the cross resonance gate, Phys. Rev. A **93**, 060302 (2016).

[3] M. Takita, A. D. Córcoles, E. Magesan, B. Abdo, M. Brink, A. Cross, J. M. Chow, and J. M. Gambetta, Demonstration of Weight-Four Parity Measurements in the Surface Code Architecture, Phys. Rev. Lett. **117**, 210505 (2016).

[4] M. Takita, A. W. Cross, A. D. Córcoles, J. M. Chow, and J. M. Gambetta, Experimental Demonstration of Fault-Tolerant State Preparation with Superconducting Qubits, Phys. Rev. Lett. **119**, 180501 (2017).

[5] N. Sundaresan, I. Lauer, E. Pritchett, E. Magesan, P. Jurcevic, and J. M. Gambetta, Reducing Unitary and Spectator Errors in Cross Resonance with Optimized Rotary Echoes, PRX Quantum **1**, 020318 (2020).

[6] A. Y. Kitaev, Fault-tolerant quantum computation by anyons, Ann. Phys. **303**, 2 (2003).

[7] C. Chamberland, G. Zhu, T. J. Yoder, J. B. Hertzberg, and A. W. Cross, Topological and Subsystem Codes on Low-Degree Graphs with Flag Qubits, Phys. Rev. X **10**, 011022 (2020).

[8] J. M. Gambetta, J. M. Chow, and M. Steffen, Building logical qubits in a superconducting quantum computing system, npj Quantum Inf. **3**, 2 (2017).

[9] G. Catelani, R. J. Schoelkopf, M. H. Devoret, and L. I. Glazman, Relaxation and frequency shifts induced by quasiparticles in superconducting qubits, Phys. Rev. B **84**, 064517 (2011).

[10] J. Koch, T. M. Yu, J. M. Gambetta, A. A. Houck, D. I. Schuster, J. Majer, A. Blais, M. H. Devoret, S. M. Girvin, and R. J. Schoelkopf, Charge insensitive qubit design derived from the Cooper pair box, Phys. Rev. A **76**, 042319 (2007).

[11] A. Blais, R.-S. Huang, A. Wallraff, S. M. Girvin, and R. J. Schoelkopf, Cavity quantum electrodynamics for superconducting electrical circuits: An architecture for quantum computation, Phys. Rev. A **69**, 062320 (2004).

[12] A. Blais, A. L. Grimsmo, S. M. Girvin, and A. Wallraff, Circuit quantum electrodynamics, Rev. Mod. Phys. **93**, 25005 (2021).

[13] F. Solgun, D. P. DiVincenzo, and J. M. Gambetta, Simple impedance response formulas for the dispersive interaction rates in the effective Hamiltonians of low anharmonicity superconducting qubits, IEEE Trans. Microw. Theory Tech. **67**, 928 (2019).

[14] J. M. Gambetta, in *Quantum Information Processing Lecture Notes*, 44th IFF Spring School 2013, Forschungszentrum Jülich.

[15] E. Magesan and J. M. Gambetta, Effective Hamiltonian models of the cross-resonance gate, Phys. Rev. A **101**, 052308 (2020).

[16] P. S. Mundada, G. Zhang, T. Hazard, and A. A. Houck, Suppression of Qubit Crosstalk in a Tunable Coupling Superconducting Circuit, Phys. Rev. Appl. **12**, 054023 (2019).

[17] F. Yan, P. Krantz, Y. Sung, M. Kjaergaard, D. L. Campbell, T. P. Orlando, S. Gustavsson, and W. D. Oliver, A Tunable Coupling Scheme for Implementing High-Fidelity Two-Qubit Gates, Phys. Rev. Appl. **10**, 054062 (2018).

[18] J. Ku, X. Xu, M. Brink, D. C. McKay, J. B. Hertzberg, M. H. Ansari, and B. L. T. Plourde, Suppression of Unwanted *ZZ* Interactions in a Hybrid Two-Qubit System, Phys. Rev. Lett. **125**, 200504 (2020).

[19] A. D. K. Finck, S. Carnevale, D. Klaus, C. Scerbo, J. Blair, T. G. McConkey, C. Kurter, A. Carniol, G. Keefe, M. Kumph, and O. E. Dial, Suppressed Crosstalk Between Two-Junction Superconducting Qubits with Mode-Selective Exchange Coupling, Phys. Rev. Appl. **16**, 054041 (2021).

[20] A. Kandala, K. X. Wei, S. Srinivasan, E. Magesan, S. Carnevale, G. A. Keefe, D. Klaus, O. Dial, and D. C. McKay, Demonstration of a High-Fidelity CNOT for Fixed-Frequency Transmons with Engineered *ZZ* Suppression, Phys. Rev. Lett. **127**, 130501 (2021).

[21] M. C. Collodo, J. Herrmann, N. Lacroix, C. K. Andersen, A. Remm, S. Lazar, J.-C. Besse, T. Walter, A. Wallraff,

and C. Eichler, Implementation of Conditional-Phase Gates based on Tunable *ZZ*-Interactions, Phys. Rev. Lett. **125**, 240502 (2020).

[22] Y. Xu, J. Chu, J. Yuan, J. Qiu, Y. Zhou, L. Zhang, X. Tan, Y. Yu, S. Liu, J. Li, F. Yan, and D. Yu, High-Fidelity, High-Scalability Two-Qubit Gate Scheme for Superconducting Qubits, Phys. Rev. Lett. **125**, 240503 (2020).

[23] Y. Sung, L. Ding, J. Braumüller, A. Vepsäläinen, B. Kannan, M. Kjaergaard, A. Greene, G. O. Samach, C. McNally, D. Kim, A. Melville, B. M. Niedzielski, M. E. Schwartz, J. L. Yoder, T. P. Orlando, S. Gustavsson, and W. D. Oliver, Realization of High-Fidelity CZ and *ZZ*-Free iSWAP Gates with a Tunable Coupler, Phys. Rev. X **11**, 021058 (2021).

[24] J. Stehlik, D. M. Zajac, D. L. Underwood, T. Phung, J. Blair, S. Carnevale, D. Klaus, G. A. Keefe, A. Carniol, M. Kumph, Matthias Steffen, and O. E. Dial, Tunable Coupling Architecture for Fixed-Frequency Transmon Superconducting Qubits, Phys. Rev. Lett. **127**, 080505 (2021).

[25] Y. Ye, *et al.*, Realization of high-fidelity CZ gates in extensible superconducting qubits design with a tunable coupler, Chin. Phys. Lett. **38**, 100301 (2021).

[26] J. Chu and F. Yan, Coupler-Assisted Controlled-Phase Gate with Enhanced Adiabaticity, Phys. Rev. Appl. **16**, 054020 (2021).

[27] K. X. Wei, E. Magesan, I. Lauer, S. Srinivasan, D. F. Bogorin, S. Carnevale, G. A. Keefe, Y. Kim, D. Klaus, W. Landers, N. Sundaresan, C. Wang, E. J. Zhang, M. Steffen, O. E. Dial, D. C. McKay, and A. Kandala, Hamiltonian Engineering with Multicolor Drives for Fast Entangling Gates and Quantum Crosstalk Cancellation, Phys. Rev. Lett. **129**, 060501 (2022).

[28] F. Solgun, in *IEEE MTT-S International Microwave Symposium (IMS)* (IEEE, Boston, USA, 2019), p. 263.

[29] Y. Chen, *et al.*, Qubit Architecture with High Coherence and Fast Tunable Coupling, Phys. Rev. Lett. **113**, 220502 (2014).

[30] M. R. Geller, E. Donate, Y. Chen, C. Neill, P. Roushan, and J. M. Martinis, Tunable coupler for superconducting Xmon qubits: Perturbative nonlinear model, Phys. Rev. A **92**, 012320 (2015).

[31] Y. Wu, W.-S. Bao, S. Cao, F. Chen, M.-C. Chen, X. Chen, T.-H. Chung, H. Deng, Y. Du, D. Fan, *et al.*, Strong Quantum Computational Advantage Using a Superconducting Quantum Processor, Phys. Rev. Lett. **127**, 180501 (2021).

[32] S. E. Nigg, H. Paik, B. Vlastakis, G. Kirchmair, S. Shankar, L. Frunzio, M. H. Devoret, R. J. Schoelkopf, and S. M. Girvin, Black-Box Superconducting Circuit Quantization, Phys. Rev. Lett. **108**, 240502 (2012).

[33] R. Winkler, in *Spin-Orbit Coupling Effects in Two-Dimensional Electron and Hole Systems* (Springer-Verlag, Berlin, Heidelberg, Germany, 2003), p. 201.